UNIVERSIDAD AUTÓNOMA DE NUEVO LEÓN
FACULTAD DE INGENIERÍA MECÁNICA Y ELÉCTRICA

TESIS

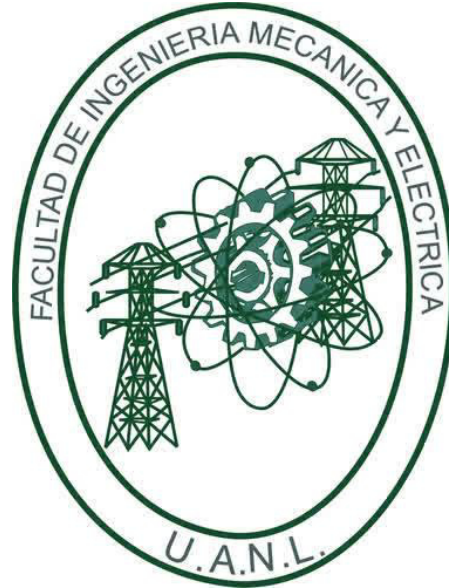**RECHAZO ACTIVO DE PERTURBACIONES EN VEHÍCULOS AÉREOS MULTIROTOR**

POR

ULISES ALVAREZ LICEAGA

COMO REQUISITO PARCIAL PARA OBTENER EL GRADO DE MAESTRÍA EN INGENIERÍA AERONÁUTICA CON ORIENTACIÓN EN DINÁMICA DE VUELO

JULIO, 2018

UNIVERSIDAD AUTÓNOMA DE NUEVO LEÓN
FACULTAD DE INGENIERÍA MECÁNICA Y ELÉCTRICA
SUBDIRECCIÓN DE ESTUDIOS DE POSGRADO

TESIS

RECHAZO ACTIVO DE PERTURBACIONES EN VEHÍCULOS AÉREOS MULTIROTOR

POR

ULISES ALVAREZ LICEAGA

COMO REQUISITO PARCIAL PARA OBTENER EL GRADO DE MAESTRÍA EN INGENIERÍA AERONÁUTICA CON ORIENTACIÓN EN DINÁMICA DE VUELO
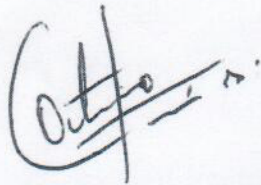
JULIO, 2018

UNIVERSIDAD AUTONOMA DE NUEVO LEON

FACULTAD DE INGENIERIA MECANICA Y ELECTRICA

SUBDIRECCIÓN DE ESTUDIOS DE POSGRADO

Los miembros del Comité de Tesis recomendamos que la Tesis **"RECHAZO ACTIVO DE PERTURBACIONES EN VEHÍCULOS AÉREOS MULTIROTOR."** realizada por el alumno(a) **"Ulises Alvarez Liceaga"**, con número de matrícula **1831338**, sea aceptada para su defensa como opción al grado de "MAESTRÍA EN INGENIERÍA AERONÁUTICA CON ORIENTACIÓN EN DINÁMICA DE VUELO".
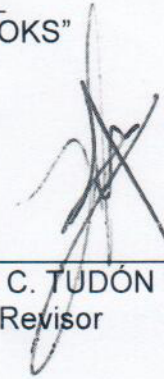
El Comité de Tesis
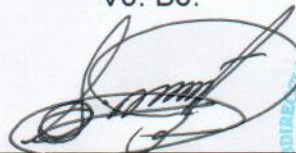
"DR. LUIS ANTÓNIO AMÉZQUITA BROOKS"
Director

DR. OCTAVIO GARCÍA SALAZAR
Revisor

DR. JUAN C. TUDÓN MARTÍNEZ
Revisor

Vo. Bo.

DR. SIMÓN MARTÍNEZ MARTÍNEZ
Subdirector de Estudios de Posgrado

San Nicolás de los Garza, Nuevo León, Julio 2018.

For my family, friends, and professors.

Índice general

Índice de figuras

ÍNDICE DE TABLAS

AGRADECIMIENTOS

Resumen

Ulises Alvarez.

Candidato para obtener el grado de Maestría en Aeronautica con orientación en Dinamica De Vuelo.

Universidad Autónoma de Nuevo León.

Facultad de Ingeniería Mecánica y Eléctrica.

Título del estudio: RECHAZO ACTIVO DE PERTURBACIONES EN VEHÍCULOS AÉREOS MULTIROTOR.

Número de páginas: 59.

OBJETIVOS Y MÉTODO DE ESTUDIO: The general objective of this thesis is to create and test a control for multirotor aircraft that is resistant to disturbances.

CONTRIBUCIONES Y CONLUSIONES: The proposed controller has the ability to be implemented into any type of multirotor vehicle.

Firma del asesor: _____

Dr. Luis Amezquita Brooks

Symbols

Abreviations

PVTOL	Planar Vertical Take-Off and Landing
IMU	Inertial Measurement Unit
PID	Proportional Integral Derivative
ADRC	Active Disturbance Rejection Control
LADRC	Linear Active Disturbance Rejection Control
LC/OFC	Linear Control
ESO	Extended State Observer
LADRCLPF	Linear Active Disturbance Rejection Control Low Pass Filter
LADRCOFCLPF	ADRC, Linear Controller, Low Pass Filter

Introduction

Small unmanned aerial vehicles (UAV) have seen a large increase in developments in the past years [2,3]. Quadrotors, specifically, have received attention due to the its simple structure. Different control strategies have been proposed to provide stabilization for the quadcopter, such as back-stepping control [7], sliding modes [6], and LQR control [5]. Although these control methods provide stability, none of them are more widely used than PID controllers [4]. However, PID controllers are susceptible to many real time issues and disturbances. For instance, the integral term of the PID introduces phase lag, and the derivative term increases the high frequency noises inherent to the inertial measurement unit (IMU). On the other hand, active disturbance rejection control (ADRC) is a strategy that can provide rejection to a wide variety of perturbations. ADRC is composed of an observer which lumps disturbances and modeling uncertainties together, such that only a simple model is required to create a robust controller [12]. ADRC has the benefit of not requiring an in-depth model, and it is easy to implement into the existing control strategy.

The purpose of this study is to create and implement an ADRC to complement linear controllers designed using classical considerations. First, a classical, linear controller will be implemented into a simplified quadcopter model, known as a Planar Take-Off and Landing Vehicle (PVTOL). This controller will then be complemented with a disturbance. This novel method can provide a stable and robust controller

Figura 1.1: Quadrotor Package Delivery Aircraft [11]

that is easy to design. More importantly, it will allow the vehicle to be less suscep-
tible to disturbances. Once the new controller is tested in simulation, the algorithm
will be uploaded to a PVTOL prototype in order to test its effectivity in real-time
conditions. Several perturbations such as uneven propellers and simulated bumps
will be analyzed.

1.1 An Introduction to Micro Aerial Vehicles

Micro air vehicles (MAV) such as fixed wing aircraft or multi-rotor craft, ha-
ve become increasingly utilized in consumer and commercial applications in recent
years. Market projections of MAVs are expected to surpass 2.2 billion dollars in 2020
[8]. This unprecedented popularity is due to several factors, such as decreasing prices
of flight components as well as the relative ease of flying an MAV. Today, MAVs are
used in a wide variety of applications ranging from acrobatics to package delivery.

1.1.1 Advantages and Disadvantages of MAVs

The popularity of MAVs is due to its myriad of advantages. First, MAVs have
high thrust to weight ratios, particularly multi-rotor vehicles. This allows them to be

able to carry heavier payloads or stronger navigational equipment, albeit over smaller distances. Second, multirotor vehicles have superior maneuverability compared to fixed wing vehicles. Quadrotor vehicles are also highly scalable, allowing the frame to be adjusted for different missions. In addition, multirotors are relatively inexpensive due to their mechanical simplicity. For example, a simple quadrotor vehicle generally only has four motors and no servos.

The main disadvantage MAVs have is their small inertial mass, which makes them susceptible to environmental perturbations. Wind gusts can easily knock a MAV off course, and even destabilize it. In addition, actuator variations such as damaged propellers can cause sudden change of behavioral characteristics.

1.2   DISTURBANCE REJECTION TECHNIQUES

Today, many different control strategies have been successfully implemented, ranging from Proportional-Integral-Derivative (PID) controllers to nonlinear methods such as sliding modes and backstepping [14]. Even though complex strategies have been successful, the prevalent control schemes are based on PIDs due to their relative simplicity and easy tuning.
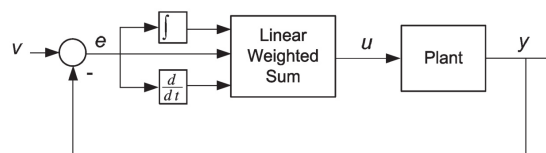
Figura 1.2: PID Control Scheme [6]

The PID control scheme, shown in fig. 1.2 has been well studied and documented in [1],[6].

Figure 1.3 shows a comparison of many different control schemes, including nonlinear approaches. The table rates the controllers on robustness, optimization,

Control Algorithm	Characteristic												
	Robust	Adaptive	Optimal	Intelligent	Tracking ability	Fast convergence/response	Precision	Simplicity	Disturbance rejection	Unmodeled parameter handling	Manual tuning	(Signal) noise	Chattering/energy loss
1. PID	1	0	0	0	1	1	1	2	0	0	2	2	0
2. Intelligent PID	1	0	0	2	1	1	1	1	0	0	0	1	0
3. LQR	0	2	1	0	1	1	0	1	1	0	1	1	0
4. LQG	0	2	2	0	1	1	0	0	2	0	1	0	0
5. L_1	0	2	2	0	1	2	2	0	1	0	0	0	0
6. H_1	2	1	2	0	2	0	1	0	1	1	0	0	0
7. SMC	1	2	1	0	2	2	2	1	2	1	0	0	2
8. FBL	1	1	0	0	2	2	2	1	1	1	0	1	0
9. Backstepping	0	2	0	0	2	0	1	0	2	1	0	0	0
10. Fuzzy logic	1	1	1	2	1	1	1	1	1	0	1	0	0
11. Neural networks	1	2	2	2	1	1	1	0	1	1	0	0	0
12. Genetic	1	2	2	2	1	1	1	0	1	2	0	0	0

Legend: 0—low to none; 1—average; 2—high. Also, 1 through 5 (Linear); 6 through 12 (Nonlinear).

Figura 1.3: Control Scheme Comparisons [14]

and other pertinent characteristics.

1.2.1 Active Disturbance Rejection Control

The following section is a short review and description of Active Disturbance Rejection Control (ADRC) as described by Han [6].

ADRC was first designed to overcome some shortcomings of PID, specifically set-point changes and disturbance issues. The resulting scheme used transient profiles and non-linear functions to eliminate overshoot. Although the controller achieved better disturbance rejection in comparison to PID, the implementation was difficult due to the large quantities of tunable parameters. For example, [2] describes the

complexity of tuning.

1.3   Problem Statement

Micro-Air Vehicles are highly susceptible to disturbances such as wind gusts and sensor noise.

1.4   Hypothesis

A linear controller coupled with ADRC method will provide adequate disturbance rejection while ensuring robustness.

1.5   Objectives

The objective of this study is to show that Active Disturbance Rejection Control in conjunction with classical control theory is a viable method to provide a stable and robust controller for a PVTOL model.

1.5.1   Specific Objectives

- Obtain a PVTOL model that adequately resembles a quadcopter.

- Design a linear controller for a obtained model.

- Design ADRC for the PVTOL.

- Analyze disturbance and noise sensitivity of obtained controllers using frequency techniques.

- Compare controllers using a simulation.

- Compare controllers using real-time experiments.

1.6   Research Methodology

To complete the main objective of the research study, several specific objectives will be introduced. An experimental procedure will be devised to complete the objectives:

- Obtain a PVTOL model that adequately resembles a quadcopter. This model should be simplified in order to conduct dynamical experiments, while being complex enough to accurately model the main quadrotor orientation dynamics.

- Design an attitude controller for the obtained linear model using classical control.

- Once the robust classical controller (in terms of classical robustness margins) is designed, a state observer will be implemented in order to determine the required variable from the inertial measurement unit (IMU).

- The controller will then be modified with ADRC. This new control will then be analyzed using frequency techniques, such as Bode plots.

- Input and noise disturbance rejection will be tuned using the same frequency techniques mentioned previously. If necessary, the noise and disturbance properties of the control will be changed using filters.

- Once a suitable controller that meets all specifications is obtained, it will be compared to other control schemes.

- A comparison will first be done in simulation. Several perturbations will be tested including sensor noise, as well as input disturbances.

- The controller will then be implemented into a PVTOL system to conduct real-time experiments. The system will also be subjected to various perturbations in order to determine real-world disturbance rejection properties.

- Data will be analyzed using box-plots to determine if the novel controller performs better than other control methodologies.

Simulation

This chapter describes the design and results of the simulation of all controllers tested.

2.1 Mathematical model

The following section succinctly describes the mathematical model used for the study.

A MAV in a quadrotor configuration can be modeled using Newton-Euler equa-
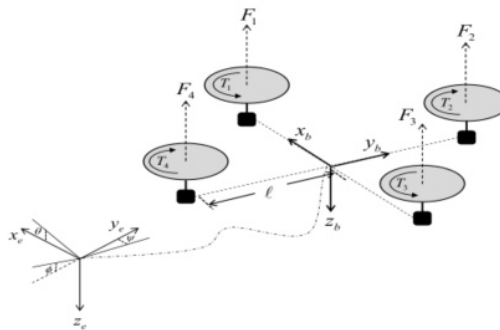

Figura 2.1: Quadrotor frame and motor configuration ([5])

tions of motion and Fig. 2.1:

$$m\dot{V}_b + m\omega_b \times V_b = F_b \tag{2.1}$$

$$J\dot{\omega}_b + \omega_b \times (J\omega_b) = M_b \tag{2.2}$$

where $V_b = \begin{bmatrix} u & v & w \end{bmatrix}^T$ and $\omega_b = \begin{bmatrix} p_b & q_b & r_b \end{bmatrix}^T$ are the linear and angular velocity vectors, F_b is the external force vector, M is the mass, J is the inertial moment matrix, and M_b is the external moment vector. If the quad-rotor body is assumed to be symmetrical, then:

$$J = diag(I_\alpha, I_\alpha, I_z) \tag{2.3}$$

where I_α is the inertial mass along x and y axes, and I_z is the inertial mass along the z axis. Considering the Euler angles $\Omega = \begin{bmatrix} \phi & \theta & \psi \end{bmatrix}^T$ with a rotation sequence $\psi - \theta - \phi$ (yaw-pitch-roll):

$$\omega_b = R_\alpha \dot{\Omega} \tag{2.4}$$

where:

$$R_\alpha{}^{-1} = \begin{bmatrix} 1 & s_\phi t_\theta & c_\phi t_\theta \\ 0 & c_\phi & -s_\phi \\ 0 & s_\phi/c_\theta & c_\phi/c_\theta \end{bmatrix}, \quad \begin{aligned} \Phi &= [\phi \ 0 \ 0]^T \\ \Theta &= [0 \ \theta \ 0]^T \\ \Psi &= [0 \ 0 \ \psi]^T \end{aligned} \tag{2.5}$$

$s_x = \sin(x), c_x = \cos(x), t_x = \tan(x)$

The thrust of the propeller can be approximated by:

$$F_i = k_p V_i^2 \tag{2.6}$$

where V is the voltage applied to the motor and k_p is a constant that can be experimentally characterized for each motor-propeller combination. Similarly, the reactive moment can be expressed as:

$$T_i = k_m V_i^2 \tag{2.7}$$

where k_m is a constant that can be that can be experimentally characterized as well.

The induced forces and moments due to thrust (2.6) and reactive moments (2.7) for an X type quadrotor are:

$$
F_\alpha^b = \begin{bmatrix} 0 & 0 & F_z \end{bmatrix}^T
$$
$$
M_\alpha^b = \begin{bmatrix} T_p & T_q & T_r \end{bmatrix}^T
$$

(2.8)

where

$$
\begin{bmatrix} F_z \\ T_p \\ T_q \\ T_r \end{bmatrix} = \begin{bmatrix} -k_p & -k_p & -k_p & -k_p \\ 0 & -\ell k_p & 0 & \ell k_p \\ \ell k_p & 0 & -\ell k_p & 0 \\ -k_m & k_m & -k_m & k_m \end{bmatrix} \begin{bmatrix} V_1^2 \\ V_2^2 \\ V_3^2 \\ V_4^2 \end{bmatrix} = P \begin{bmatrix} V_1^2 \\ V_2^2 \\ V_3^2 \\ V_4^2 \end{bmatrix}
$$

(2.9)

Combining (2.8) and (2.4), we obtain the following simplified model ([1]):

$$
\ddot{\varphi} = \dot{\theta}\dot{\psi}\left(\frac{I_\alpha - I_z}{I_\alpha}\right) + \frac{1}{I_\alpha}T_p
$$

$$
\ddot{\theta} = \dot{\varphi}\dot{\psi}\left(\frac{I_z - I_\alpha}{I_\alpha}\right) + \frac{1}{I_\alpha}T_q
$$

(2.10)

$$
\ddot{\psi} = \dot{\varphi}\dot{\theta}\left(\frac{I_\alpha - I_\alpha}{I_z}\right) + \frac{1}{I_z}T_r
$$

In [5] and [1], the process for further simplification of the orientation model is shown. This results in the following transfer matrix:

$$
\begin{bmatrix} \theta(s) \\ \phi(s) \\ \psi(s) \end{bmatrix} = diag \begin{bmatrix} \frac{1}{I_\alpha s^2} & \frac{1}{I_\alpha s^2} & \frac{1}{I_z s^2} \end{bmatrix} \begin{bmatrix} T_p \\ T_q \\ T_r \end{bmatrix}
$$

(2.11)

The preceding model shows that the attitude angles are decoupled. Therefore, each angle can be studied separately with a planar vertical take off and landing (PV-TOL) model, as shown in the following figure. This model will be used in simulation as well as real-time experiments.

The PVTOL model has three output variables, (x, y, ψ), which correspond to the x position, y position, and ψ angular position around the origin in the xy plane.
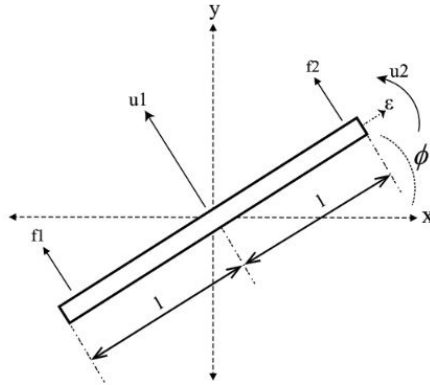
Figura 2.2: PVTOL Schematic [3]

The model has two control inputs, (f_1, f_2), which correspond to the thrust generated by the two motors. The distance to the center of gravity is l. The two input forces can be described as a singular accumulated force acting on the center of mass of the vehicle:

$$u_1 = f_1 + f_2 \tag{2.12}$$

The resulting moment of u_1 can be expressed as:

$$u_2 = (f_2 - f_1)\, l \tag{2.13}$$

In addition, the force the motor and propeller assembly produce can be roughly described as:

$$f_i = k_p V_i \tag{2.14}$$

where V_i is the voltage applied to the motor, and k_p is a propeller constant that is experimentally characterized.

Using the definitions of 2.12 and 2.14, the mathematical model of the system

is:

$$m\ddot{x} = u_1 \sin \phi - \varepsilon u_2 \cos \phi$$
$$m\ddot{y} = -u_1 \cos \phi - \varepsilon u_2 \sin \phi - mg \qquad (2.15)$$
$$I\ddot{\phi} = u_2$$

where ε is the coupling coefficient, m is the mass of the vehicle, I is the moment of inertia, and g is gravitational acceleration [3].

Since the PVTOL is restricted to rotation around the center of mass of the vehicle, the resulting model can be described as:

$$I\ddot{\phi} = (f_2 - f_1)\, l - b\dot{\phi} \qquad (2.16)$$

where b is a friction coefficient of the fixed rotational point. If b is assumed to be small, the plant of the PVTOL results in:

$$G(s) = \frac{\theta(s)}{T_x(s)} = \frac{1}{I_x s^2} \qquad (2.17)$$

where I_x is the inertial mass along the specified axis.

Note that model 2.17 is similar the model of one orientation axis of the quadrotor (eq.2.11). This similarity allows studiying some of the MAV orientation dynamics using the simplified PVTOL prototype.

2.2 CLASSICAL LINEAR CONTROL

It is well known that classical linear control, in particular if designed using frequency analysis tools, allows proper assessment of the robustness and performance. For instance, using the nominal system model (2.11), a set of linear controllers was designed using Bode shaping techniques for the pitch, roll, and yaw angles. The detailed design procedure for pitch and roll angles are presented as an example. The

same procedure can also be utilized for the design of the yaw angle controller, albeit with a different inertial coefficient.

2.2.1 Linear Controller Design

Due to the symmetry of the vehicle, the pitch and roll dynamics are similar, thus the same controller can be used for both. Controller (2.18) was designed for pitch and roll of the simplified model (2.11) considering the specifications in Table.2.1 and Table.2.2.

Table 2.1: Control Design Specifications

	Specification	Proposed Control
Bandwidth	2-10 rad/s	5 rad/s
Phase Margin(M_p)	>60 deg	78.6 deg
Gain Margin(M_g)	>12dB	-inf dB

Table 2.2: Air Vehicle Parameters

Inertia I_α	.0049 kgm^2
Inertia I_z	.0088 kgm^2
b_α	204.0816
l	.225 m

$$OFC(s) = \frac{1.225(s + 0.5)}{(s + 50)} \qquad (2.18)$$

The nominal robustness and performance properties can be derived from the Bode plot shown in Fig. 2.3.

Designing a classical controller guarantees proper performance and robustness. However, it will be shown that this controller is highly sensitive to input disturbances.
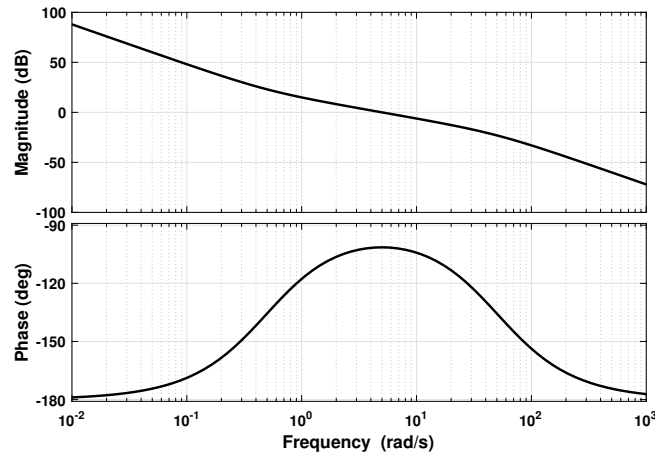
Figura 2.3: Open loop Bode Plot pitch and roll dynamics using controller (2.18)

One method to improve this problem is to increase the controller gain at lower frequencies. Nonetheless, this would also introduce phase lag, which can compromise the robustness and transient responses [10].

In the following sections a novel control scheme that combines the input disturbance properties of linear ADRC and the performance and robustness of classical control is presented.

2.3   Linear Active Disutrbance Rejection Control

Implementation of a second order ADRC has already been well studied ([7], [2], [13]). The central idea is to use an extended state observer (ESO) to estimate the internal and external disturbances in real time. Originaly, ADRC had complex tuning parameters as well as nonlinear gains. However, in [4], the authors implemented ADRC using a linear observer, which simplified the implementation without compromising its performance and robustness, as shown in fig. 2.4.
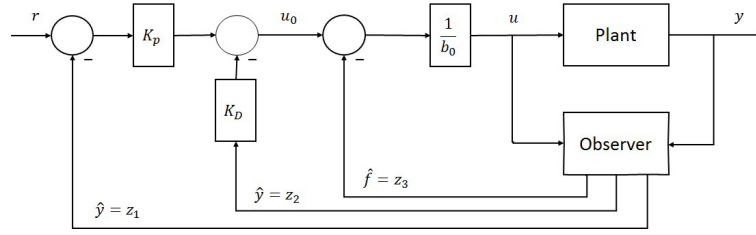
Figura 2.4: Linear ADRC with complete state feedback

A basic presentation of linear ADRC, as proposed in [4] is presented next for a second-order system . A general second-order plant is considered as:

$$\ddot{y} = g(y, \dot{y}, w, t) + bu \tag{2.19}$$

where y is the system output, u is the control signal, b is a constant, and w represents external disturbances. ADRC treats $g(y, \dot{y}, w, t)$ as the generalized disturbance, which is denoted as $f(t)$. This generalized disturbance is estimated using an ESO. If $x_1 = y, x_2 = \dot{y}, x_3 = f$, the second-order plant can be represented with a state space model as shown below:

$$\dot{x} = Ax + Bu + Ef$$
$$y = Cx \tag{2.20}$$

where:

$$A = \begin{bmatrix} 0 & 1 & 0 \\ 0 & 0 & 1 \\ 0 & 0 & 0 \end{bmatrix}, B = \begin{bmatrix} 0 \\ b \\ 0 \end{bmatrix} E = \begin{bmatrix} 0 \\ 0 \\ 1 \end{bmatrix} \tag{2.21}$$

and $C = \begin{bmatrix} 1 & 0 & 0 \end{bmatrix}$. Using the classical Luenberger equations for system (2.19), the ESO results in:

$$\dot{z} = Az + Bu + L(x_1 - z_1)$$
$$\hat{y} = Cz \tag{2.22}$$

where the observer gain vector L is chosen so that all the observer eigenvalues are located at $-\omega_0$ ([13]).

$$L = \begin{bmatrix} 3\omega_0 & 3\omega_0^2 & \omega_0^3 \end{bmatrix}^T \tag{2.23}$$

If the observer is well tuned, and the disturbance signals are bounded and continuous, it can be assumed that z_1, z_2, and z_3 closely track $y, \dot{y}$, and f respectively. Then control law

$$u = \frac{(u_0 - z_3)}{b} \tag{2.24}$$

reduces (2.19) to an approximated double integrator plant.

$$\ddot{y} = f + u_0 - z_3 \approx u_0 \tag{2.25}$$

The closed loop dynamics of (2.25) are then adjusted by using the complete state feedback:

$$u_0 = k_p(r - z_1) - k_d z_2 \tag{2.26}$$

where k_p and k_d are controller gains which are set according to the formulas described in [7].

Using the model described in table 2.2, the following table shows the resulting LADRC gain values and pole placement:

Table 2.3: LADRC Control
LADRC Control Parameters

Cutoff Frequency	-5 rad/s
Observer Poles	[-15 -75 -125]
k_p	36
k_d	12

The use of ADRC imparts good input perturbation rejection characteristics and when no perturbation is present, the performance and robustness properties are similar to typical state-feedback control.

Notwithstanding the attractive input perturbation rejection properties of ADRC, in the following sections it will be shown that the noise sensitivity of this scheme is high, limiting the usefulness of this scheme.

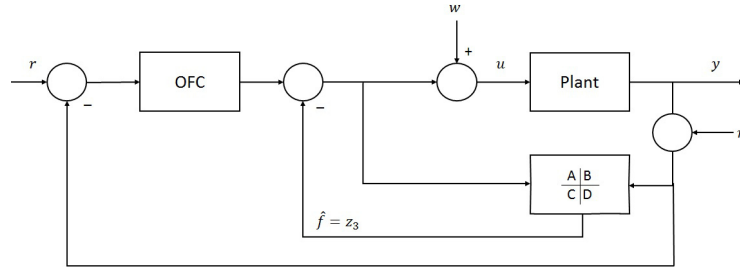## 2.3.1   A MODIFIED ADRC WITH CLASSICAL CONTROL

Figura 2.5: Scheme combining OFC and ADRC

In contrast to the implementation of ADRC, only the estimation of the disturbance will be used in conjunction with a nominal control $(OFC(s))$ designed using frequency domain specifications. That is, the estimated lumped disturbance, z_3, will be used in conjunction with the linear controller described in (2.18). The resulting scheme is shown in Fig. 2.5 and will be denoted as OFC+ADRC. The quadrotor model (2.11) is first expressed as a state space model. In this configuration, it is typical that two output variables are measured using an inertial measurement unit (IMU) to estimate angular positions. In particular, the accelerometer of an IMU are used to reconstruct angular position, while the gyroscopes measure angular velocities. Therefore, for the ADRC observer both outputs are used, while the linear controller OFC only utilizes angular position feedback. As follows the integration of the ADRC observer with the OFC will be explained. Consider a second degree system with a linear observer:

$$
\begin{pmatrix} \dot{x}_1(t) \\ \dot{x}_2(t) \\ \dot{x}_3(t) \end{pmatrix} = A \cdot \begin{pmatrix} x_1(t) \\ x_2(t) \\ x_3(t) \end{pmatrix} + B \cdot u(t) + E \cdot \dot{f}(t)
$$
$$
y(t) = C \cdot \begin{pmatrix} x_1(t) \\ x_2(t) \\ x_3(t) \end{pmatrix}
$$

(2.27)

where

$$A = \begin{pmatrix} 0 & 1 & 0 \\ 0 & 0 & 1 \\ 0 & 0 & 0 \end{pmatrix}, B = \begin{pmatrix} 0 \\ b \\ 0 \end{pmatrix}, E = \begin{pmatrix} 0 \\ 0 \\ 1 \end{pmatrix}$$
$$C = \begin{pmatrix} 1 & 0 & 0 \\ 0 & 1 & 0 \end{pmatrix} \tag{2.28}$$

The resulting ESO is:

$$\dot{\hat{X}} = (A - LC)\hat{X} + \begin{bmatrix} B & L \end{bmatrix} \begin{bmatrix} u(t) \\ y(t) \\ \dot{y}(t) \end{bmatrix} \tag{2.29}$$

where $L = \begin{bmatrix} l_{11} & l_{12} \\ l_{21} & l_{22} \\ l_{31} & l_{32} \end{bmatrix}$

Summarily, the state space matrices of the ADRC observer yield:

$$A_{Obs} = \begin{bmatrix} -l_{11} & 1-l_{12} & 0 \\ -l_{21} & -l_{22} & 1 \\ -l_{31} & -l_{32} & 0 \end{bmatrix}, B_{Obs} = \begin{bmatrix} 0 & l_{11} & l_{12} \\ b & l_{21} & l_{22} \\ 0 & l_{31} & l_{32} \end{bmatrix}$$
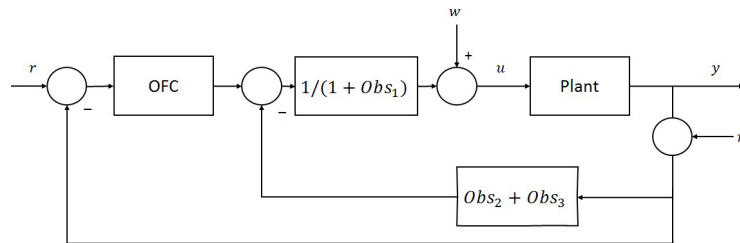$$C_{obs} = \begin{bmatrix} 0 & 0 & 1 \end{bmatrix} \tag{2.30}$$

Figura 2.6: Linear Controller and ADRC

To analyze the effects of the coupling of ADRC with the linear controller, the

Laplace transform of the state observer was taken. That is:

$$
\begin{aligned}
z_3(s) &= C_{Obs}(sI - A_{Obs})B_{Obs}\begin{bmatrix} u(s) & y(s) & \dot{y}(s) \end{bmatrix}^T \\
&= \begin{bmatrix} Obs_1 & Obs_2 & Obs_3 \end{bmatrix}\begin{bmatrix} u(s) & y(s) & \dot{y}(s) \end{bmatrix}^T
\end{aligned} \tag{2.31}
$$

Making the proper block algebra simplifications, the final proposed control scheme is shown in Fig. 2.6, where:

$$
\begin{aligned}
Obs_1 &= -\frac{\frac{b}{l_{32}}(s+(l_{31}+l_{11}l_{32}-l_{21}l_{31})l_{22})}{A_1} \\
Obs_2 &= \frac{s\left(s+\frac{l_{22}l_{31}-l_{21}l_{32}}{l_{31}}\right)}{A_1} \\
Obs_3 &= \frac{l_{32}s^2+(l_{11}l_{32}-l_{12}l_{31})s+(l_{21}l_{32}-l_{22}l_{31})}{A_1}
\end{aligned} \tag{2.32}
$$

and $A_1 = s^3 + (l_{11} + l_{22})s^2 + (l_{21} + l_{32} + l_{11}l_{22} + -l_{12}l_{21})s + (l_{31} + l_{11}l_{32} - l_{12}l_{31})$.

As follows it will be shown that in nominal conditions; without perturbation, the resulting closed loop response depends only on the linear controller (OFC(s)). This implies that the ADRC component does not affect the performance and robustness provided by the linear controller. According to Fig. 2.5, in nominal conditions, the resulting transfer fuction which models the closed loop response is given by:

$$
\frac{y(s)}{r(s)} = \frac{OFC(s)Obs_{loop}(s)}{1 + OFC(s)Obs_{loop}(s)} \tag{2.33}
$$

where

$$
Obs_{loop}(s) = \frac{\frac{G(s)}{1+Obs_1}}{1 + \left(\frac{G(s)(Obs_2+Obs_3)}{1+Obs_1}\right)}
$$

Substituting eq. (2.32) into (2.33) it turns out that:

$$
\frac{y(s)}{r(s)} = \frac{OFC(s)G(s)}{1 + (OFC(s)G(s))} \tag{2.34}
$$

which is equal to the closed loop transfer function if only the OFC controller is considered.

This is a key result as it shows that the effect of the ADRC observer is separable from any linear feedback controller in closed loop if only the perturbation rejection component of ADRC is used.

2.3.2   Pole Placement Analysis

In [13], a simple method for selecting the ADRC observer gains is presented. This method can be used when the measured variable is a scalar signal. However, due to the air vehicle system having a two dimensional measurement vector, the method proposed in ([13]) cannot be applied directly. Therefore, a pole placement algorithm was used to set the poles at different frequencies, as shown in Fig.2.7 and Fig.2.8.
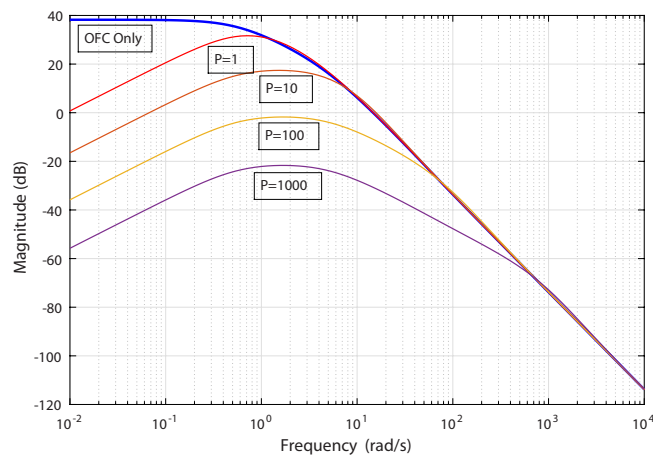

Figura 2.7: Input Disturbance Sensitivity of $OFC(s)G(s)$ and $(OFC + ADRC)G(s)$

Fig. 2.7 shows the sensitivity to input disturbances of the OFC and $OFC + ADRC$ control schemes. It is clear that the $OFC + ADRC$ combination greatly improves the sensitivity to low frequency input disturbances compared to the standalone OFC scheme. In addition, it can be seen that as the observer poles increase the input disturbance sensitivity decreases. This result is in line with the expected behavior of the disturbance observer: increasing the observer performance improves the input disturbance rejection.

Fig. 2.8 shows the sensitivity to sensor noise of the OFC and $OFC + ADRC$ control schemes. In contrast to the input perturbation rejection, the system is more susceptible to high frequency sensor noise as the observer poles frequency increases.
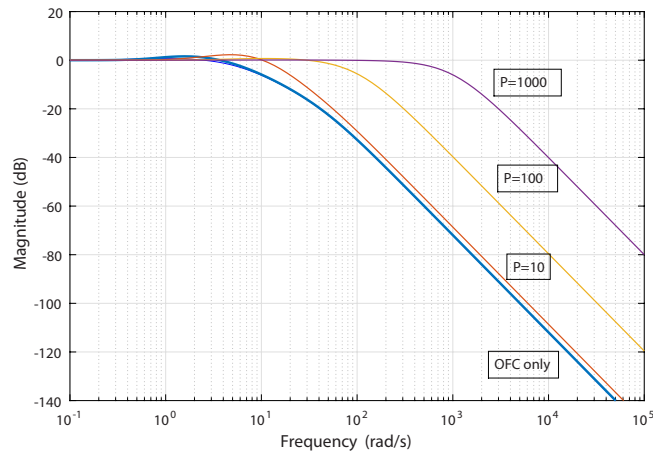
Figura 2.8: Noise Sensitivity of $OFC(s)G(s)$ and $(OFC + ADRC)G(s)$

This higher sensitivity is especially detrimental as IMU measurements contain a significant amount of high frequency noise. Lowering ADRC observer pole values reduces noise sensitivity; however, the attractive input disturbance properties are negatively impacted.

2.3.3   Observer Gain Analysis

As discussed in [6], ADRC has a described method for choosing an appropriate gain vector depending on the desired bandwidth. However, this procedure is only described for single input, single output systems.

2.3.3.1   Empirical Adjustment

As the method for choosing appropriate gains is not defined, the first step was to find acceptable observer poles, which is shown in the previous section. From eq.

2.29, we obtain:

$$\dot{\hat{x}} = \begin{bmatrix} -L_{11} & 1-L_{12} & 0 \\ -L_{21} & -L_{22} & 1 \\ -L_{31} & -L_{32} & 0 \end{bmatrix} \hat{x} + \begin{bmatrix} 0 & L_{11} & L_{12} \\ b_0 & L_{21} & L_{22} \\ 0 & L_{31} & L_{32} \end{bmatrix} \begin{bmatrix} u \\ \hat{x}_1 \\ \hat{x}_2 \end{bmatrix} \tag{2.35}$$

The determinant of the matrix

$$\begin{bmatrix} s+L_{11} & L_{12}-1 & 0 \\ L_{21} & s+L_{22} & -1 \\ L_{31} & L_{32} & s \end{bmatrix} \tag{2.36}$$

is

$$\lambda = s^3 + a_2 s^2 + a_1 s + a_0 \tag{2.37}$$

where

$$\begin{aligned} a_2 &= L_{22} + L_{11} \\ a_1 &= L_{32} + L_{22}L_{11} - L_{21}L_{12} + L_{21} \\ a_0 &= L_{11}L_{32} - L_{12}L_{31} + L_{31} \end{aligned} \tag{2.38}$$

Since there are only 3 equations and 6 variables, some gains were chosen as constants.

Using the observer poles obtained in the previous section, the gains were modulated in order to perceive their effect on disturbance and noise sensitivity. Figures 2.9 and 2.10 show the effects of L_{32} gain modulation. This specific gain had the most dramatic impact on the sensitivities, as can be especially seen in fig. 2.9. Note that a small gain ($L_{32} \leq 1$), does not further affect disturbance: $L_{32} = 1$ (red) is similar to $L_{32} = 0.1$ (blue) . Additionally, it is readily observable that as the gain is reduced, the sensitivity to input disturbance is also reduced. Increasing the gain has a highly detrimental effect to input disturbance rejection, making the LADRC control perform worse than the nominal LC controller.

Figure 2.10 shows that modulating the L_{32} gain also impacts noise sensitivity. Having a high gain creates an unusable controller due to high noise sensitivity.
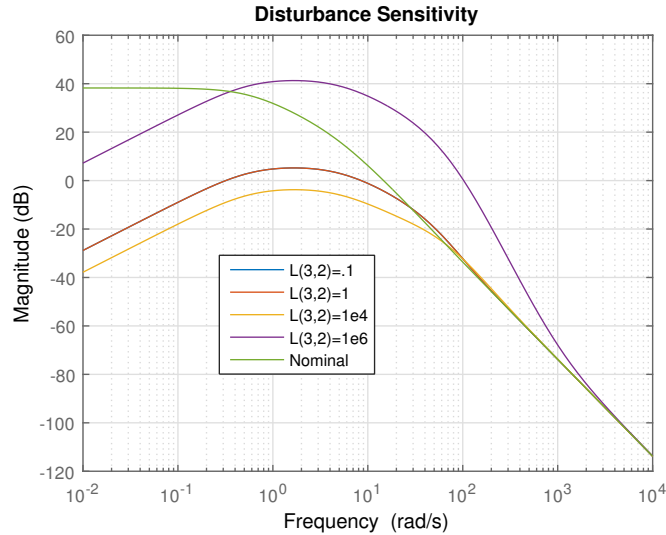
Figura 2.9: L_{32} Gain Input Disturbance

Additionally, it can be observed that having a gain less than 1 does not provide additional noise rejection.

2.3.4   LOW PASS FILTER-ADRC COMBINATION

The previous results suggest that the selection of the ADRC observer gains should be made considering a compromise between sensor noise and input perturbation rejection. In current literature, there are several methods which could be potentially used for this purpose, such as optimal control theory. In the following section, a simple approach for adjusting the resulting sensor noise sensitivity is presented. This method is based on introducing a low pass filter within the ADRC transfer functions in order to cutoff the bandwidth of the observer. The resulting scheme is shown in Fig. 2.11.

Fig. 2.12 shows the sensitivity to sensor noise of the OFC scheme compared to that of the OFC+ADRC using the proposed LPF. The filter cutoff frequencies considered are: $\omega_c = [1, 10, 15, 30] rad/s$. From this figure, it is clear that as the
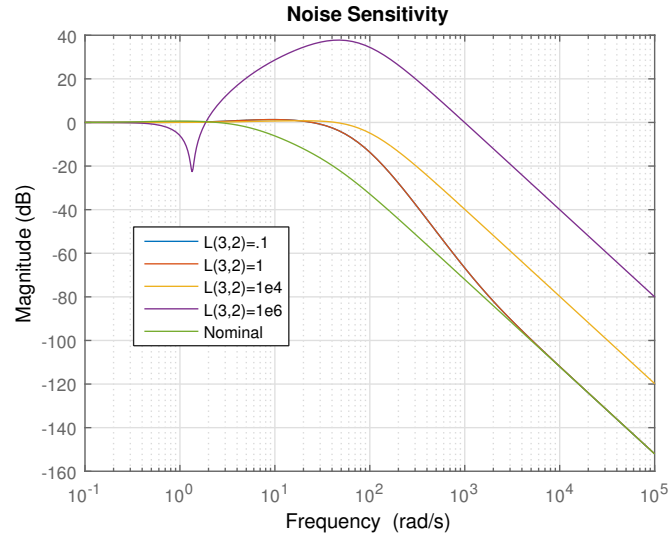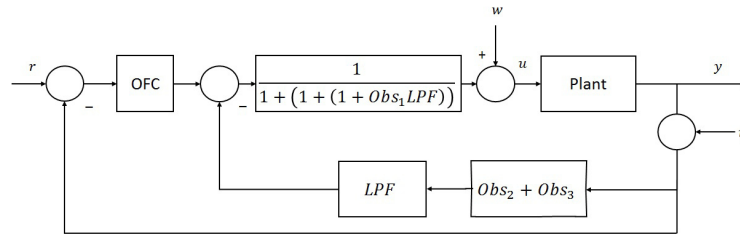
Figura 2.10: L_{32} Gain Noise Disturbance

Figura 2.11: OFC + ADRC with Low Pass Filter

LPF cutoff frequency decreases, the sensor noise sensitivity improves.

On the other hand, the frequency of the LPF also affects the input disturbance rejection, as shown in Fig. 2.12. As the LPF cutoff frequency decreases, the input disturbance rejection deteriorates. Nonetheless, in all cases the input disturbance rejection at lower frequencies is significantly better than that of the OFC scheme.

An important observation from Figs. 2.12 and 2.13 is that for low ω_c values, the filter begins to interfere with the dynamics of $OFC(s)G(s)$, introducing a phase lag in the open loop transfer function, causing a large unwanted peak. This is also indicative of a reduced level of robustness. Therefore, a LPF cutoff frequency higher
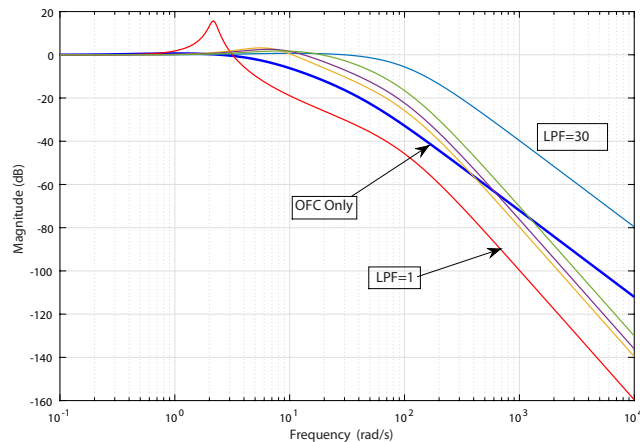
Figura 2.12: Sensor Noise Sensitivity of $OFC(s)G(s)$ and $(OFC + ADRC + LPF)G(s)$

than the nominal open loop bandwidth is indicated in order to avoid this problem.

From Figs. 2.13 and 2.12, it can be concluded that adding a low pass filter adds a new parameter for tuning the level of ADRC disturbance rejection and sensor noise sensitivity, simplifying the task of achieving the required specifications. Although a similar result can be reached by proper tunning of the ADRC observer gains, the introduction of the LPF has a clear and unique effect,making it simpler to adjust. Finally, it should be noted that the proposed scheme allows achieving good levels of sensor noise and input perturbation rejection for high and low frequency bands respectively. However, the cross-over frequency band is still vulnerable to these perturbations. This is a well known limitation which applies to all control schemes ([10]).

2.4   PID Control

Proportional-Integral-Derivative (PID) control is a commonly used controller scheme for quad-rotors due to its relatively simple tuning method, as well as easy im-
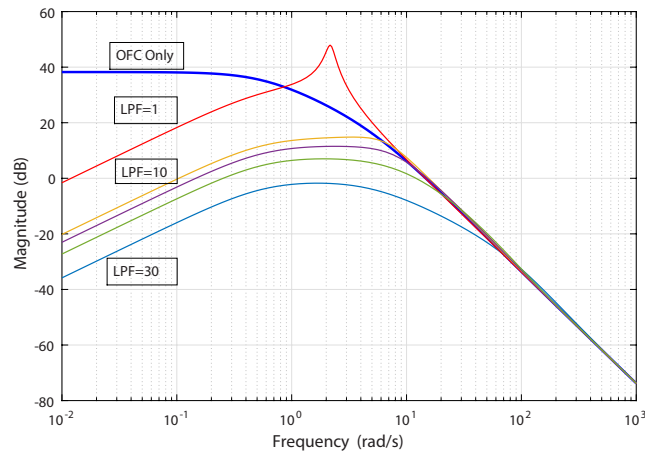
Figura 2.13: Input Disturbance Sensitivity of OFC and OFC+ADRC using the LPF at several cut frequencies

Table 2.4: PID Control Parameters

PID Controller Parameters

k_p	.5
k_i	.04
k_d	.1
n	100

plementation. The PID controller was tuned in order to conform to the specifications described in table 2.1.

Table 2.4 shows the final values obtained for the PID controller. The parameter n is a pole at $s = -100$ that serves to reduce high frequency effects exacerbated by the derivative term of the controller.

$$C_{PID}(s) = \frac{0.1(s + 4.919)(s + 0.08132)}{s} \qquad (2.39)$$

The PID controller proposed in eq.(2.39) meets all of the specifications of a robust controller, as shown in fig.2.14. However, the PID may not conform to our
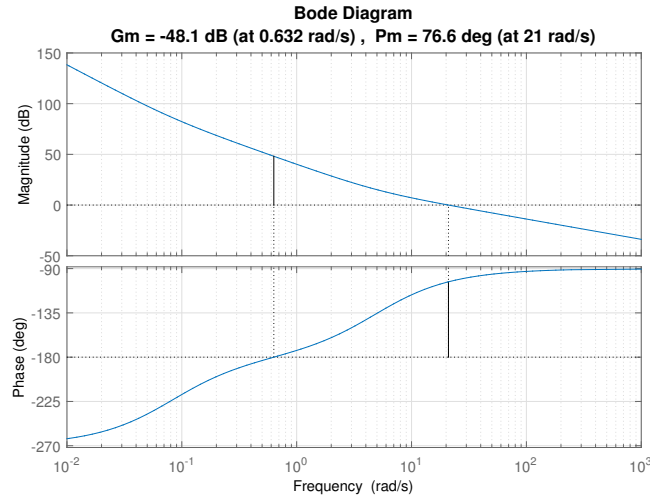
Figura 2.14: Open loop Bode Plot of pitch and roll dynamics using PID controller

proposed disturbance rejection criteria, as shown below.
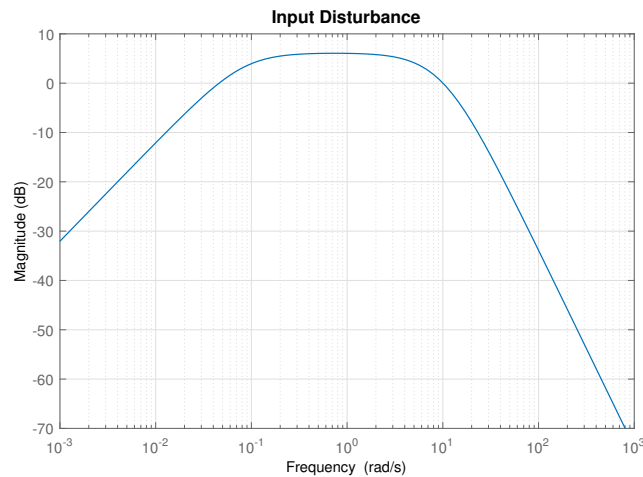

Figura 2.15: Input Disturbance Magnitude

Figure 2.15 shows the effects of input disturbance on the PID controller. As can be observed, the controller is susceptible to disturbances in a frequency range from .1 to 10 rad/s. The sensitivity in this large region is critical, since the PVTOL model proposed is very simplified. If there are any plant differences in this frequency band, the controller will be less effective.
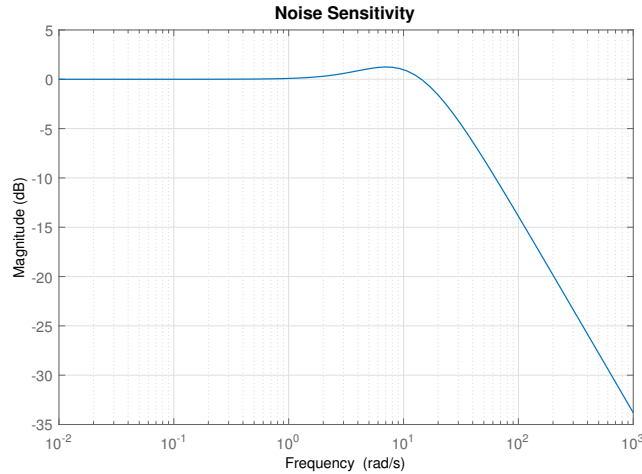
Figura 2.16: Noise Sensitivity Magnitude

Noise sensitivity, as shown in Fig. 2.16, is acceptable, but worse in comparison to other control schemes proposed. Additionally, the sensitivity is greater than $0dB$ in the $3 - 10rad/s$ frequency region.

2.5 NOISE REDUCTION DISTURBANCE OBSERVER

Another control scheme, based on a disturbance observer, was also studied in order to compare to the proposed LADRCLPF controller. In [9], a modified disturbance observer named noise reduction disturbance observer (NR-DOB) is implemented. This control strategy claims to attenuate measurement noise as well as input disturbance. This is achieved by using a low pass filter (referred to as the Q-filter), to separate high frequency noise (ω_H) from low frequency noise (ω_L), as shown in eq. (2.40).

$$\begin{aligned} |Q(j\omega)| &\approx 1, \qquad \omega \in [0, \omega_L] \\ |Q(j\omega)| &\approx 0, \qquad \omega \in [\omega_H, \infty) \end{aligned}$$

(2.40)

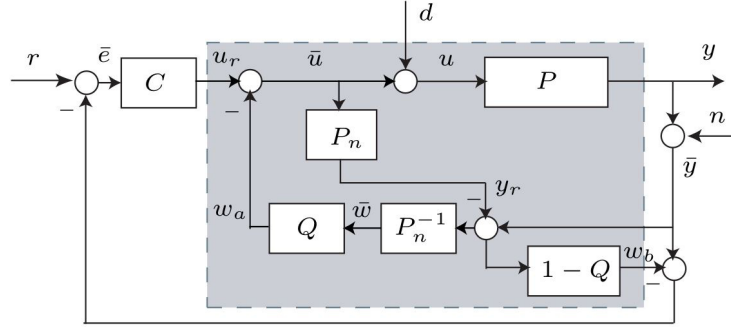Figure 2.17 shows the resulting control scheme, where signals r, d, n respectively

Figura 2.17: Noise Reduction Disturbance Observer (NR-DOB) [9]

represent the reference input, input disturbance, and noise. $P(s)$ represents the plant, whereas P_n represents the nominal model, and $C(s)$ is a linear controller which is designed using the same methods as shown in Section 2.2.

From Fig. 2.17, the plant output is:

$$y(s) = T_{yr}(s)r(s) + T_{yd}(s)d(s) - T_{yn}(s)n(s) \tag{2.41}$$

where

$$
\begin{aligned}
T_{yr}(s) &= \frac{P_n P C}{(1+P_n C)(P_n + Q(P-P_n))}, \\
T_{yd}(s) &= \frac{P_n P(1-Q)}{P_n + Q(P-P_n)}, T_{yn}(s) = \frac{P(Q)}{P_n + Q(P-P_n)}
\end{aligned}
\tag{2.42}
$$

In the low frequency range $[0, \omega_L]$:

$$|T_{yr}(j\omega)| \approx \left| \frac{P_n C}{1+P_n C}(j\omega) \right|, |T_{yd}(j\omega)| \approx 0, |T_{yn}(j\omega)| \approx 1 \tag{2.43}$$

which results in the output:

$$y(j\omega) \approx \frac{P_n C}{1+P_n C}(j\omega) \cdot r(j\omega)on \tag{2.44}$$

This is a particularly important result, as it means that NR-DOB controller scheme does not affect the nominal response of the system if there are no disturbances and/or plant uncertainties at low frequencies.

For high frequency noises $[\omega_H, \infty)$,

$$|T_{yr}(j\omega)| \approx \left|\frac{PC}{1+P_nC}(j\omega)\right|, \quad |T_{yd}(j\omega)| \approx |P(j\omega)|, \quad |T_{yn}(j\omega)| \approx \left|\frac{PQ}{P_n}(j\omega)\right| \qquad (2.45)$$

From eq.2.45, it can be readily seen that the noise can be attenuated by a well tuned Q filter.

The robustness and stability of the disturbance observer is further discussed in [12], as well as in [9].

Using the framework described above, a NR-DOB control scheme was implemented in order to provide a comparison.

In this simulation, the nominal plant and the actual plant $G(s)$ were assumed to be identical. However, one of the criteria of NR-DOB controller is that the plant must be stable. Since the PVTOL system is critically stable with two poles at the origin, then an inner control loop is considered so that the effective plant $P(s)$ becomes

$$P_n(s) = P(s) = \frac{G(s)C(s)}{1 + G(s)C(s)} \qquad (2.46)$$

where $G(s)$ is the plant shown in eq.(2.17) and $C(s)$ is the linear controller designed in the previous section.

The Q-filter, which is a low-pass filter, was selected as

$$Q(s) = \frac{10^4}{(s + 10)^4} \qquad (2.47)$$

Finally, the controller $C_n(s)$ was designed to meet the specifications defined in Table. 2.1.

$$C_n(s) = \frac{s + 5}{s} \qquad (2.48)$$

2.5.1   Disturbance and Noise Sensitivity of NR-DOB

In order to fully appreciate the comparison between NR-DOB and LADRCLPF, the sensitivity to noise and input disturbance were analyzed. Both control schemes advertise the ability to attenuate both noise and input disturbance, however, their methods are distinct and different.
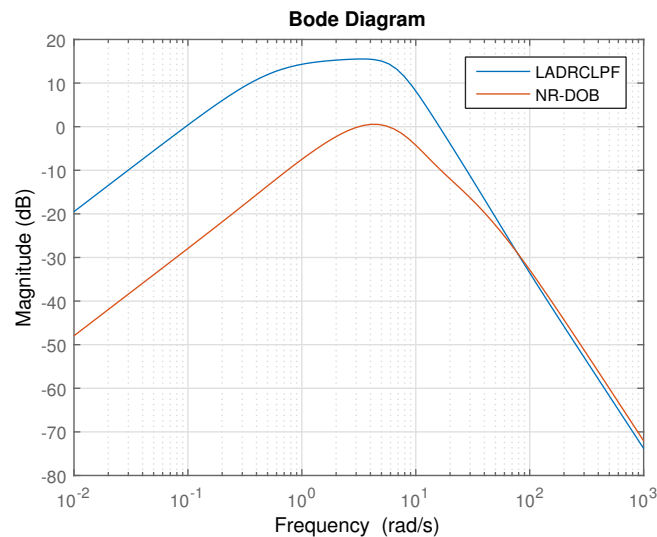

Figura 2.18: Input Disturbance Sensitivity Comparison

Fig. 2.18 shows the disturbance sensitivity of the LADRCLPF and NR-DOB control schemes. The LADRCLPF shown in this comparison hast the poles and gains set as described in section 2.34. Furthermore, the low pass filter was set at $10rad/s$. It is readily visible that NR-DOB has a large advantage in rejecting input disturbances. For example, at the operating bandwidth of $1 - 10rad/s$, NR-DOB sensitivity is at $0dB$ or below, while LADRCLPF has a sensitivity above $10dB$.

Additionally, Fig. 2.19 shows the difference between noise sensitivities of LADRC-LPF and NR-DOB control schemes. Both methods are adequate in rejecting high frequency noise. From these graphs, it is apparent that NR-DOB is an effective tool that rivals ADRC. However, the NR-DOB controller represents the "best case
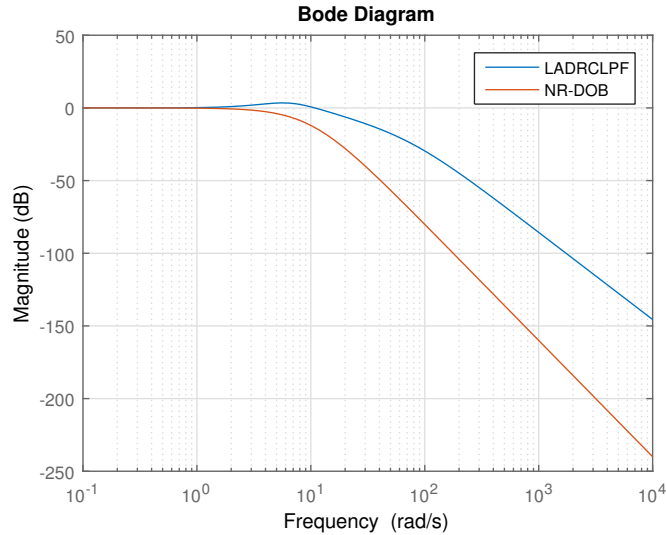
Figura 2.19: Noise Sensitivity Comparison

scenario."Specifically, it is assumed that the nominal plant and the real plant are identical, which is an improbable assumption. The analysis of these issues are further explained in [9].

2.6 Nominal Simulation Results

In this section, the controllers were simulated in nominal conditions. That is, no input or disturbances were added. The step response figure is shown below.

As expected, the LC, LADRCOFC, and LADRCLPF control schemes respond identically under nominal operation. The PID controller has slightly larger overshoot, while the LADRC has a typical damped behavior.

Figure 2.21 shows a comparison of the total error of the different control schemes. The boxplot is an effective in showing the strengths and weaknesses of the control schemes. It can be clearly seen that LADRC performs best in nominal conditions. Another important observation is that LC, LADRCOFC, and LADRCLPF
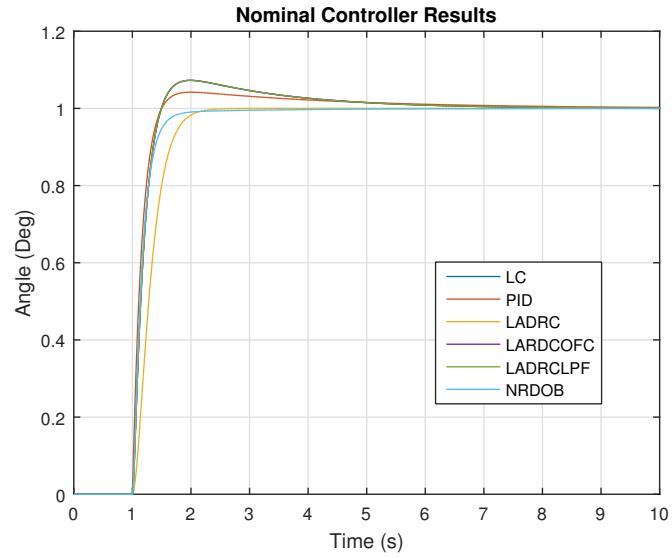
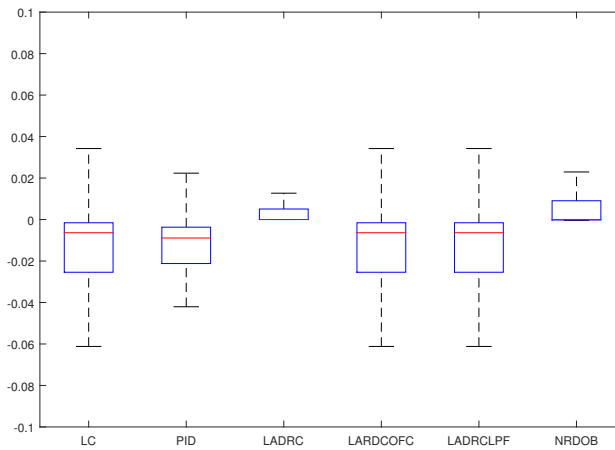Figura 2.20: Nominal Control Simulation Results

Figura 2.21: Nominal Control Simulation Error Boxplot

perform identically when there is no disturbance present. This confirms the findings in section 2.34.

2.7   DISTURBANCE SIMULATION RESULTS

2.7.1   INPUT DISTURBANCE RESULTS

In this section, the controllers were simulated with a pseudo-random input disturbance filtered with a first-order low pass filter at $0.1rad/s$. In addition to showing the susceptibility to low frequency perturbations, this simulation can help to see the effects of model uncertainties as well as certain parameter changes.
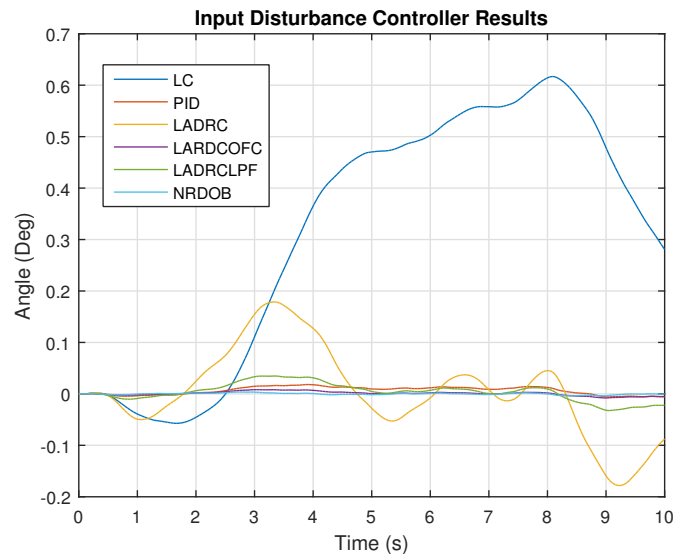

Figura 2.22: Input Disturbance Control Simulation Results

Figure. 2.22 shows that both LC and LADRC are highly affected by input disturbances, which was predicted by the bode plots shown in the previous section. Particularly, LC has large angular variations up to 0.6 degrees. In contrast, the PID, LADRCLPF, and NRDOB controls are able to effectively reject the input disturbance. This result can be easier seen in the boxplot below.

Figure 2.23 clearly shows that the LC is the poorest performing controller with respect to input disturbances, followed by LADRC. On the other hand, LADRCOFC,
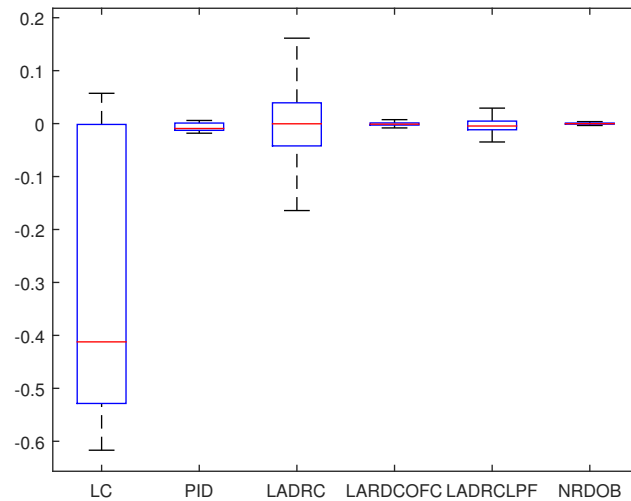
Figura 2.23: Input Disturbance Control Simulation Error Boxplot

LADRCLPF, PID, and NRDOB are very effective in this regard. Note that although NRDOB seems to be the best performing controller in this aspect, it is operating in the best case scenario.

2.7.2 Sensor Noise Disturbance Results

In this section, the controllers were simulated with a pseudo-random noise disturbance filtered with a high pass filter at $10rad/s$. In real world operation, the PVTOL can experience noises in this range due to the sensors. Therefore, it is imperative that the control schemes do not adversely affect the performance of the plant.

Figure. 2.24 shows the results of the simulation. Although the graph is cluttered, it can be readily seen that the LADRCOFC is highly susceptible to noise. This controller would be unsuitable for use in the PVTOL. However, with the addition of the low pass filter, the effect of noise is minimized. LC, PID, LADRC, and NRDOB are not as effected as the previous controls, which can be readily seen in the boxplot
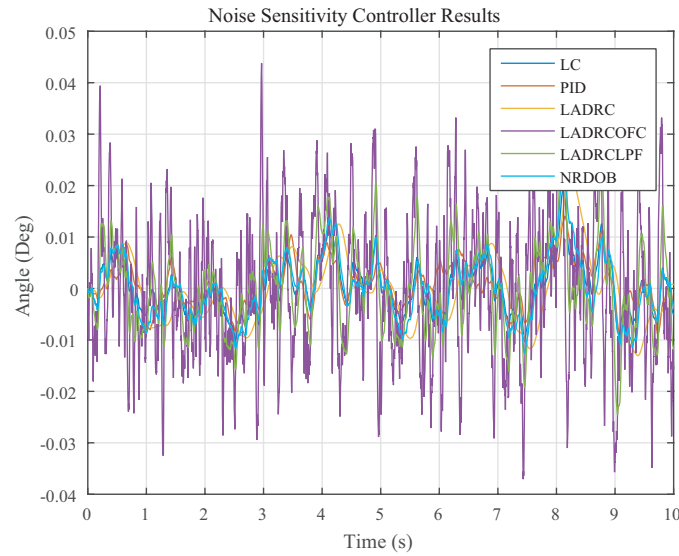
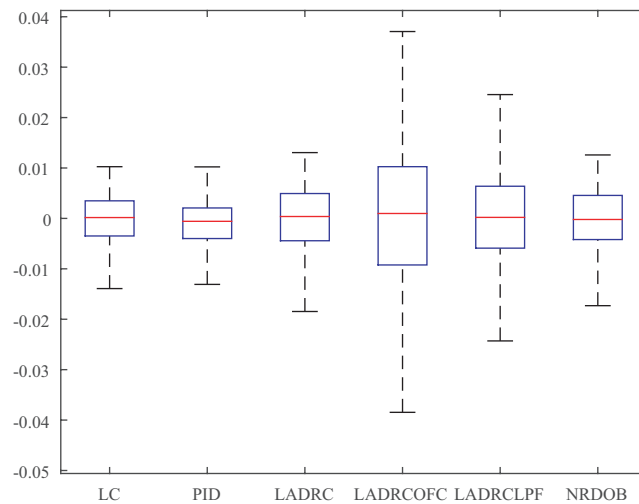Figura 2.24: Sensor Noise Disturbance Simulation Results

shown below.

Figura 2.25: Noise Disturbance Error Boxplot

Figure 2.25 affirms that LADRCOFC has poor noise disturbance rejection. However, all other controllers are within an acceptable range. It is also clear that the low pass filter added to LADRCOFC is effective in reducing the effect of noise.

2.7.3 COMBINED DISTURBANCE RESULTS

Finally, a simulation with both input and noise disturbances is shown below. As stated previously, the purpose of the study is to create a controller that is capable of rejecting both types of perturbations. For this purpose, both an input disturbance at low frequency (filtered at $0.1 rad/s$) as well as noise filtered at $10 rad/s$ was added to the system.
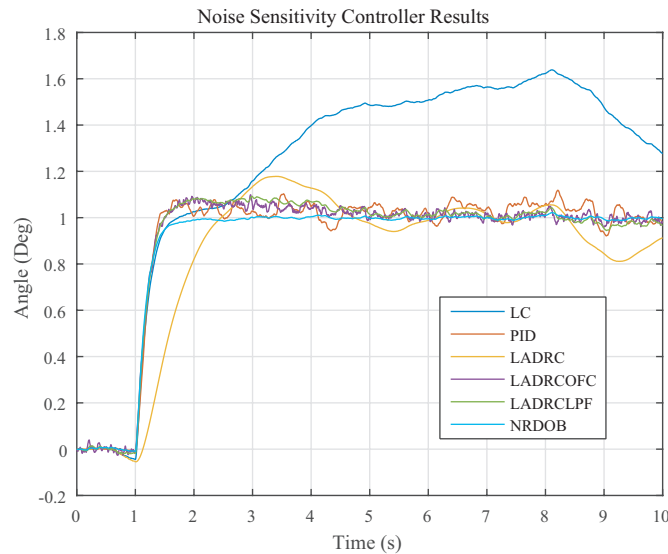

Figura 2.26: Simulation Results

Figure. 2.26 shows that both LC and LADRC have poor disturbance rejection due to their inability to reject input perturbations. However, all other controls perform very similarly. One surprising result is that PID starts to perform worse than the other proposed controls.

The results can also be summarized by Figure. 2.27, which is a boxplot of the error of each control-plant scheme. Although PID, LADRCOFC, and LADRCLPF seem to perform similarly, it is important to note that LADRCOFC is much more susceptible to noise, which is present in the actual system. Again, NRDOB seems to be the best performing controller in an ideal simulation, but it must be remembered
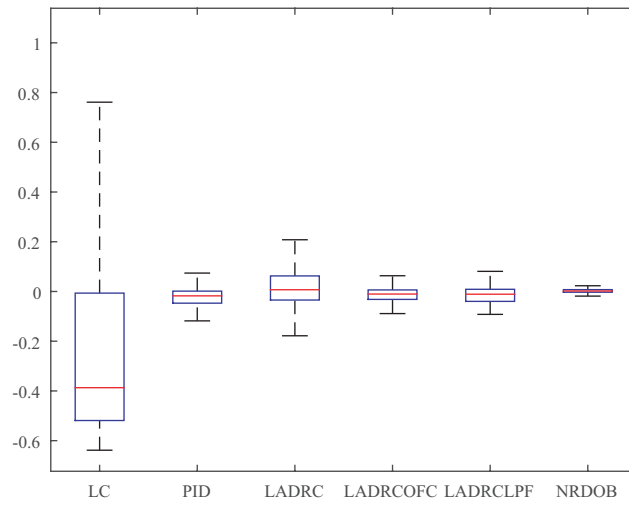
Figura 2.27: Simulation Error Boxplot

that it was designed assuming no plant uncertainties.

Real Time Experimentation

This section presents the results of real time experiments. The first tests performed were to examine the nominal operation of the system. After the behavior was analyzed, different perturbations were added, both in simulation and introducing changes to the physical plant. Three control methods were tested, PID, LC, and LADRCLPF.

3.1   PVTOL Platform

In order to test the different control schemes a PVTOL platform, designed in a previous research study was used. A succinct description of the platform is given in this section.

The PVTOL test bench (fig. 3.1) is primarily constructed with aluminum beams. It can be used to characterize and validate control systems for UAVs in real time. The test bench is also compatible with wind tunnels. It is fully instrumented with a 9 DOF IMU as well as a Texas Instruments micro-controller. The test bench can be used to solve the following problems: characterization of propulsion systems, validation of system avionics and navigation, and characterization of wind gust effects. The test bench is also reconfigurable, in order to better resemble a wider
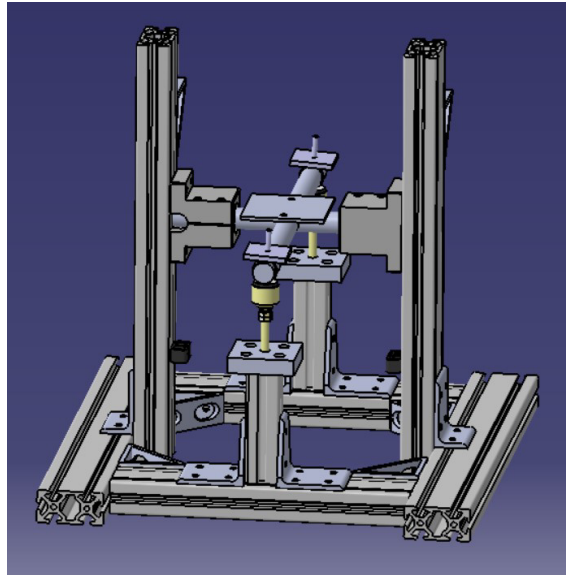
Figura 3.1: CAD Drawing of PVTOL Test Platform

range of UAV configurations.

3.1.1   PVTOL Platform Instrumentation

The test bench was configured with the following parts:

- 2 980kv brushless motors

- 2 8x4 propellers

- 2 10x6 propellers

- 2 30A Electronic Speed Controllers (ESC)

- 1 MPU6050 Inertial Measurement Unit (accelerometer, gyroscope, magneto-meter, and altimeter)

- 1 Texas Instruments C2000 Piccolo Microcontroller

- Wireless transmitter and receiver

- 2 Low friction ball bearings

- 1 3S 11.1V Li-Po battery

3.2   Control Implementation

To design and implement the different control schemes, Matlab Embedded Coder$^{\text{TM}}$ was used to create a code compatible with the TI microcontroller architecture.

3.2.1   PVTOL Characterization

As shown previously, the simplified mathematical model of the PVTOL results in a double integrator plant eq. (2.16). To find the correct gain of the system, a step sequence reference of $+/-8$ degrees was inputed into the model using a simple PID controller designed experimentally (see section 3.2.2).
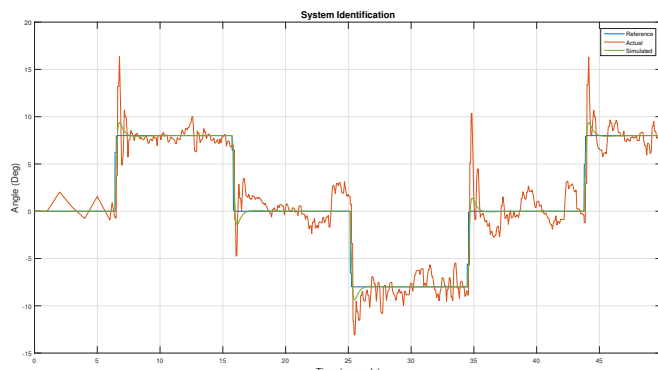

Figura 3.2: PVTOL Characterization

Fig. 3.2 shows the results of the PVTOL characterization. The graph shows the pitch angle response of the system subjected to a step reference of 8 degrees. The step reference inputed was of 8 seconds in order for the system to completely

complete its transient phase. Furthermore, a negative step reference was also tested in order to test negative angles of the system. This was done to test whether or not the system was balanced. From the recorded input and output signals, it was found that the gain of the system was 900, resulting in the experimental model:

$$G(s) = \frac{900}{s^2} \tag{3.1}$$

Fig. 3.2 also shows additional unidentified dynamics. For instance, it is possible to see an imbalance between positive and negative movements of the PVTOL. This could be due to imbalances in the weight of the PVTOL arms, motor misalignment or mistimed electronic speed controls. Furthermore, there is a large amount of noise that could be attributed to many factors. For example, the test was conducted near a solid flat surface. This means that the experiments can be effected by ground effect, which is very difficult to model. Notwithstanding, the model is still valid and can be used to design controllers for the system and good robustness margins can be considered.
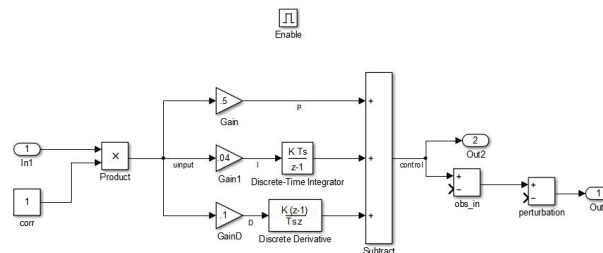
3.2.2   PID Control

Figura 3.3: PID Code

Fig. 3.3 shows the result of the implementation of a PID control scheme. The control parameters obtained are described in the following table:

Table 3.1: PID Parameters

PID Control Values	
P	.5
I	.04
D	.1
n	100

The parameters shown in table 3.1 were obtained experimentally, as opposed to following any formal guidelines. This was done because most quadrotor PID controls are tuned experimentally in the field. Therefore, the PID obtained would more closely resemble an actual control that could be used in typical applications.
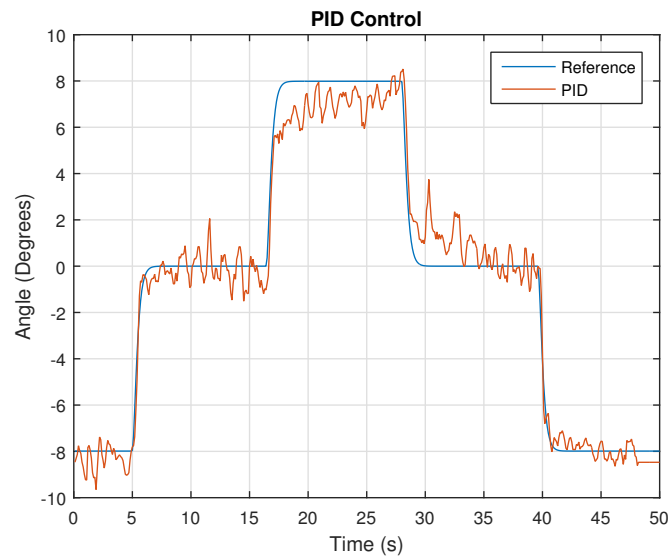

Figura 3.4: PID Control Nominal Results

Fig. 3.4 shows the result of the PID control in nominal conditions with a pre-filter. The PID control is effective in reaching the setpoint. In addition, the control is very easy to tune, with only three changeable parameters. However, the derivative gain is limited due to the high frequency sensor noise. Increasing this gain further would introduce oscillations that would destabilize the system.
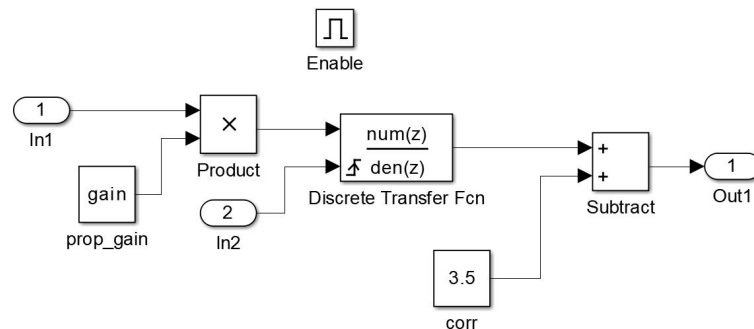
3.2.3   Linear Control

Figura 3.5: Linear Control Code

Figure 3.5 shows the linear control code that was implemented. One important observation is the addition of a corrective input offset in order for the control to reach the desired equilibrium point. This is due to the control not having an integrator and unbalances in the PVTOL. However, near zero error is obtainable with trial and error in nominal operation.
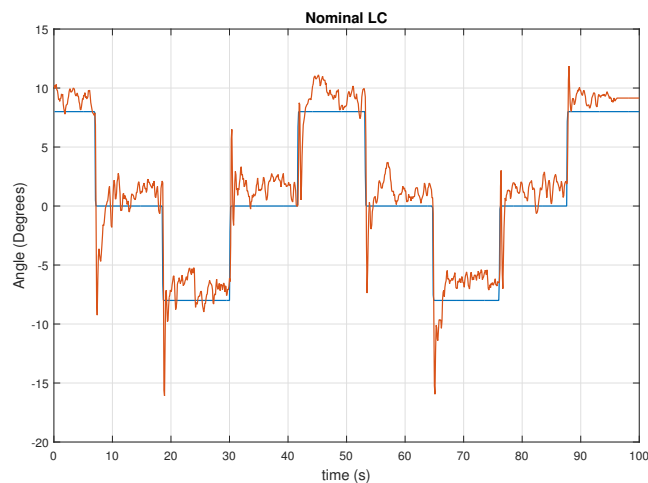

Figura 3.6: Nominal LC Graph

Figure 3.6 shows the results of the LC control in nominal operation. The output is similar to PID, however, with fewer and tighter oscillations.
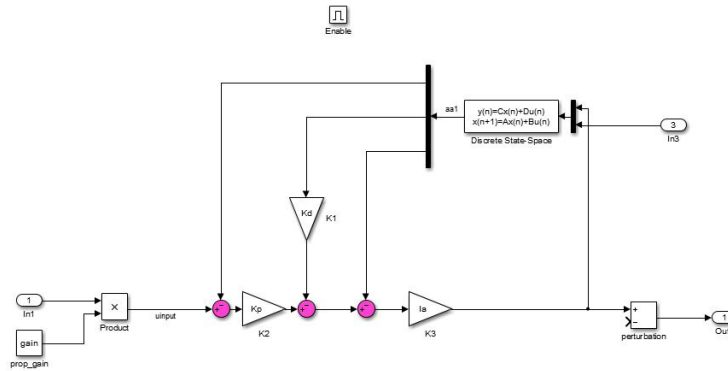
3.3 Active Disturbance Rejection Control

Figura 3.7: LADRC Code

A canonical ADRC with full observer feedback was also programed for comparison with the modified LC+ADRCLPF control scheme. The parameters used are shown in the following table (note that the poles are located according with the suggestion which accompany canonical ADRC):

Table 3.2: LADRC Control
LADRC Control Parameters

Cutoff Frequency	-5 rad/s
Observer Poles	[-15 -75 -125]
K_p	36
K_d	12

Fig. 3.8 shows the result of the Canonical ADRC control in nominal operation. The control is easy to tune, but does not meet the set point. This is possibly due insufficient Kp gain. It is also possible that this control also requires a correction factor, such as the LC control. However, the structure of canonical ADRC is rigidly defined, and was kept for illustrative purposes. In addition, there are some errors resulting in peaks of up to 2 degrees. This control method is also highly susceptible to set point changes, resulting in the problematic peaking phenomenon.
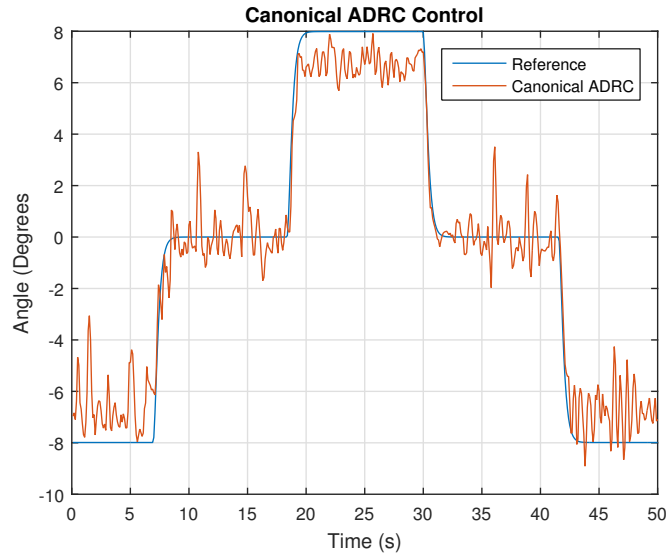
Figura 3.8: Canonical ADRC Control Nominal Results

3.3.1 LC+ADRCLPF Control
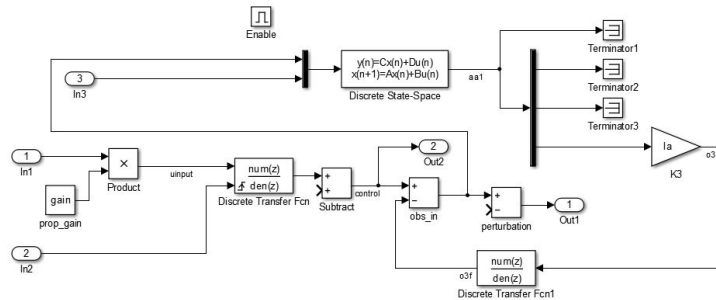

Figura 3.9: LC+ADRCLPF

Figure 3.9 shows the programmed result of the LC+ADRCLPF control scheme. The final parameter values, which were tuned experimentally, are identical to the ones obtained in the simulation

An important observation is that the gains selected in the simulation were the ones that were used in real-time experiments. The only parameter that was adjusted was the low pass filter. This is a great result for two reasons. First, the control is easy

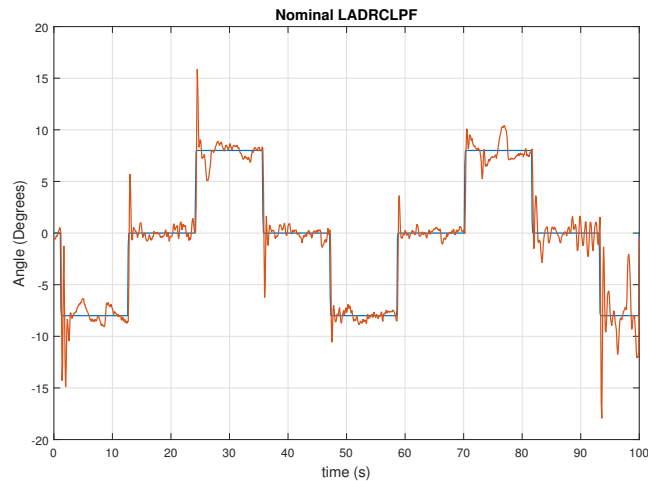to tune with minimal adjustments. Second, the control can be further fine-tuned by adjusting the gains.

Figura 3.10: ADRCLPF Nominal (no pre-filter)

Fig 3.10 shows the result of the ADRCLPF control in nominal operation. This control scheme combines the tuning ease of the linear controller and the benefits of the disturbance rejection of ADRC. Furthermore, this control method is less susceptible to set point changes, as opposed to the canonical ADRC which uses full state feedback. However, large peaks are still present, which could be reduced further by proper reference signal conditioning (i.e using a prefilter) as will be demonstrated in section 3.3.3.

3.3.2   Nominal Results Analysis

As in the previous section, the controls were compared with a box plot in order to ascertain the differences in disturbance rejection. Figure 3.11 confirms that the ADRCLPF control performs better than the other controls tested, both with less error and smaller deviation. For instance, it can be seen that the LC algorithm did not have zero error, as its boxplot is centered around 1.8 degrees. Furthermore, the
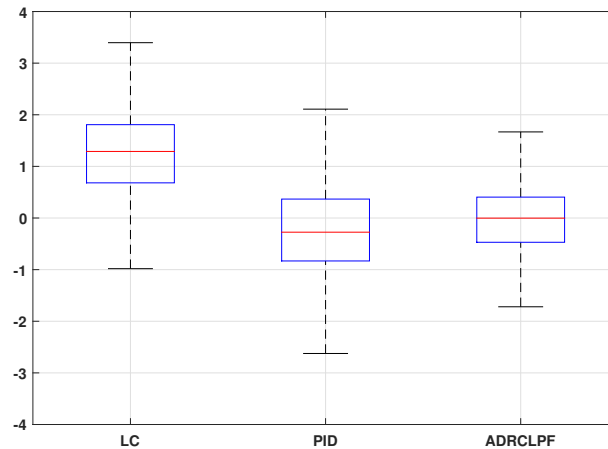
Figura 3.11: Nominal Control Error Comparison

ADRCLPF control is the most successful in attaining minimal error.

3.3.3   Pre-filter

As shown in the previous section, the ADRCLPF control has substantial overshoot due to changes in set point. One method of removing this problem is to apply pre-filter compensation.

$$PF(s) = \frac{25}{(s+5)^2} \tag{3.2}$$

The pre-filter was then applied to the reference signal, as shown in configuration figure below.

In fig. 3.12, $C(s)$ represents the control algorithms and $G(s)$ denotes the plant. $PF(s)$ was then tuned experimentally by analyzing the response of the system.

Figure 3.13 illustrates the drastic difference that the pre-filter causes. Instead of having large peaks of around 8 degrees as seen in fig.3.10, the pre-filter effecti-
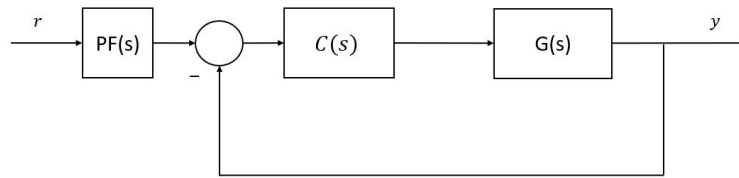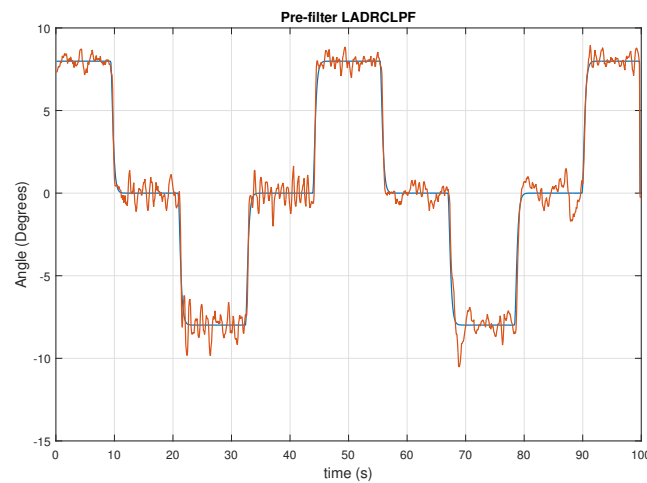
Figura 3.12: Pre-filter Configuration

Figura 3.13: ADRCLPF with Pre-filter

vely eliminates the overshoot. This pre-filter was used for the rest of the real-time experiments, as transient performance was not greatly affected.

3.3.4   Disturbance Experiments

In this section, the system was subjected to two different types of disturbances: a simulated perturbation and disparate (uneven) propellers. These tests were conducted in order to test the efficacy of disturbance rejection of each control.

3.3.4.1 Simulated Disturbance Signal

The first disturbance tested consisted of a step signal with a frequency of 3 seconds. This disturbance is added directly to the input of the system.
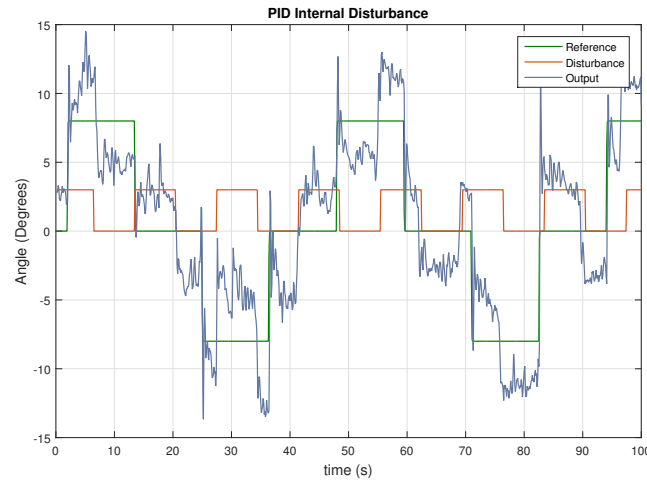

Figura 3.14: PID Internal Disturbance

Fig. 3.14 shows the results of adding a simulated disturbance to the system with PID control. The signal in red represents the step perturbation that was coded into the algorithm. It is evident that the control has poor disturbance rejection. Furthermore, it is unable to converge onto the reference signal.

In stark contrast, the ADRCLPF control adequately rejects the programmed disturbance signal. Although the perturbation causes very large peaks, the control is able to reject the signal and return to the reference point.

In order to further illustrate the difference between the controls, a box plot comparison is shown in fig. 3.16. The PID control is unable to achieve zero error, as opposed to the ADRCLPF control. Furthermore, the ADRCLPF control has a smaller deviation in comparison to the PID. However, certain outliers shown in 3.16 show that there are significantly large peaks caused by the disturbance.
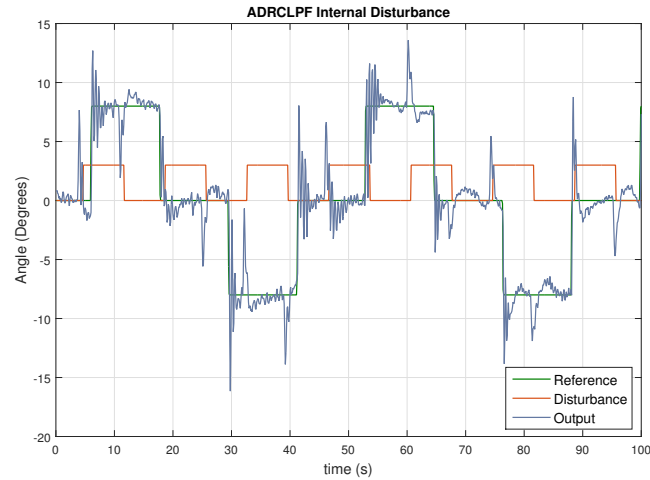
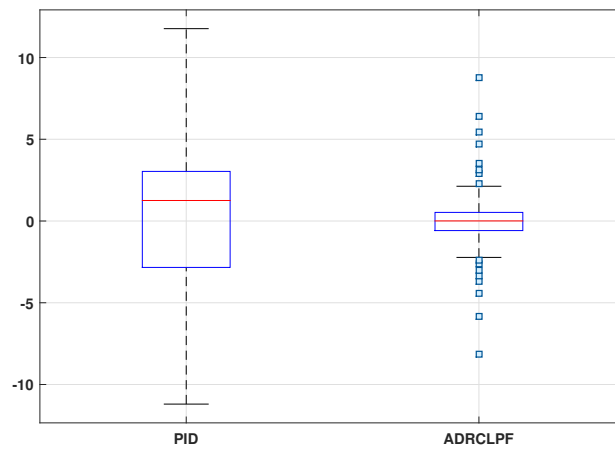Figura 3.15: ADRCLPF Internal Disturbance

Figura 3.16: Internal Disturbance Boxplot

3.3.4.2   UNEVEN PROPELLERS

The final disturbance test was to change one propeller of the PVTOL to a large one (10 inch Vs. 6 inch), changing the weight distribution of the PVTOL as well as the thrust. Changing the propeller effectively increases the thrust of one motor compared to the other.
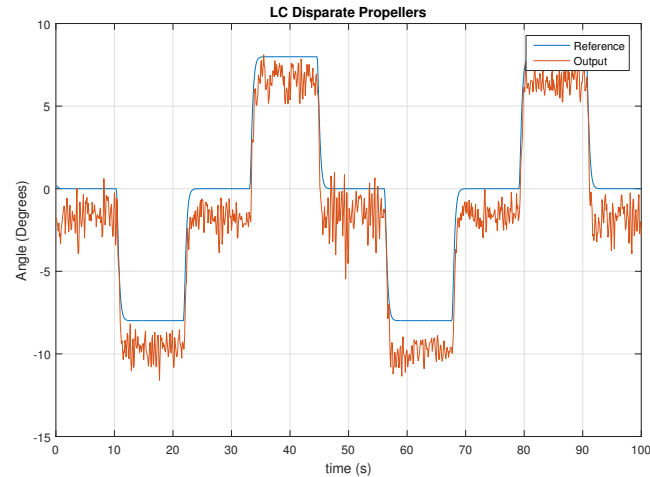
Figura 3.17: LC Uneven Propellers

Figure. 3.17 shows the results of the uneven propeller disturbance with the LC algorithm. The results look similar in comparison to nominal conditions, however, with important differences. Again, the reference is never met, and is further offset than in nominal conditions. Another difference is that the uneven motor thrust causes more oscillations, which can be seen in fig. 3.17.
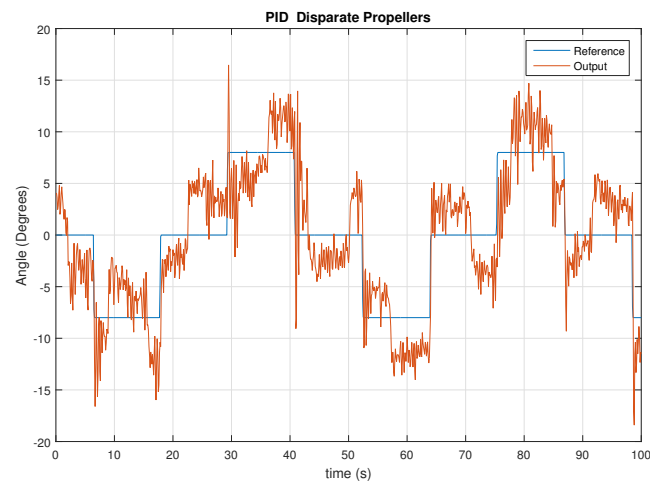
Figura 3.18: PID Uneven Propellers

Figure 3.18 shows the results of the disturbance experiment with the PID

control algorithm. Again, the control is unable to reject the disturbance, and becomes erratic.
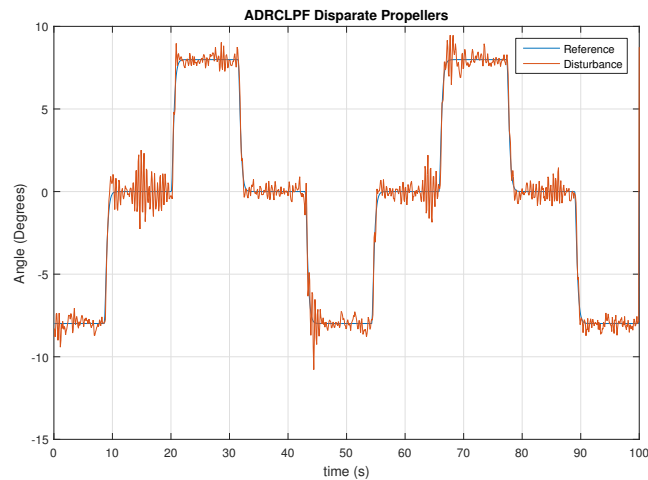
Figura 3.19: ADRCLPF Uneven Propellers

In contrast, fig. 3.19 shows the result of the disturbance study applied to the ADRCLPF algorithm. The control code is highly effective in removing the effects of the perturbation. The output follows the reference, with minimal overshoot in set-point changes. Some large oscillations can be seen, as in $t = 10 : 20s$.

Figura 3.20: Uneven Propellers Error

Fig. 3.20 further demonstates the effectiveness of the ADRCLPF algorithm. The total error of the ADRCLPF controller is closer to zero as opposed to the other controllers. The LC and PID controls do not achieve zero error. Furthermore, ADRCPLPF has the smallest whiskers, indicating that the system did not deviate from the reference as much as the other controls.

CONCLUSIONS

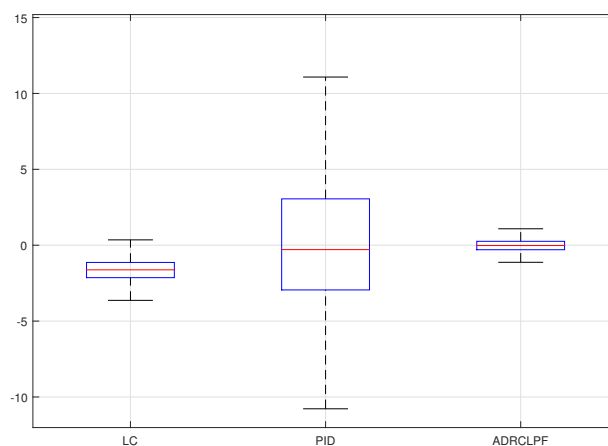In conclusion, a new control method that provides adequate input and noise disturbance rejection for multirotor vehicles was designed. The controller was compared to other similar control methods in order to gage its properties. The results of this comparison are shown succinctly in tables 4.1 and 4.2.

The ADRCLPF controller proved to be an effective method for minimizing disturbances. In addition, ADRCLPF is simple to design due to first creating a linear controller and then adding ADRC. This design method also has the benefit of using well-known stability and performance criteria in order to fully analyze and tune the controller. Furthermore, ADRCLPF is adequate at both disturbance and noise rejection.

Table 4.1: Tested Controls

Tested Controls				
	PF	**Ease of Design**	**N. Rej.**	**D. Rej.**
PID	4	5	1	2
LC	5	5	3	3
CanLADRC	3	4	5	5
ADRCLPF	3	4	5	5
NrDOB	-	3	-	-

Table 4.2: Tested Controls Cont.

Tested Controls		
	Implementation	**Tunable**
PID	5	5
LC	5	5
CanLADRC	4	4
LCADRC	4	5
NrDOB	2	3

Table 4.1 and table 4.2 describe the strength and weaknesses of all the tested controllers on a scale of 1 to 5 where 1 is the worst and 5 is the best. The first category, pre-filter, describes the necessity of having a pre-filter. Some controllers, such as ADRC, are highly susceptible to abrupt set-point changes, which cause a large overshoot, while others, such as the linear controller, are more tolerant to reference changes. The second category describes the ease of design. Controllers such as PID have tried and tested design methodologies; in contrast, NrDOB has less strict design rules which require further testing in order to achieve an adequate controller. Implementation of the controllers are also compared. Again, PID and LC are more easily discretized as opposed to ADRC and NrDOB. Finally, controller tuneability is also compared. Some controllers such as PID are very easy to tune, while others, such as NrDOB have many changeable parameters. Although having many parameters increases tunability, more time has to be spent in experimentation and analysis in order to find an appropriate solution.

4.0.1   Future Work

Future work can be completed in several different sections:

- Further analysis of gain matrix and pole placement for ADRC.

- Analysis of observer error estimation.

- Implementation of ADRCLPF in a quadrotor vehicle.

- Wind tunnel "gust"disturbance testing.

- Further tuning of PVTOL model and system identification.

Bibliografía

[1] Bai, Y., H. Liu, Z. Shi y Y. Zhong, «Robust control of quadrotor unmanned air vehicles», en *Chinese Control Conference*, IEEE, págs. 4462–4467, 2012.

[2] Chen, X., D. Li, Z. Gao y C.-W. , «Tuning method for second-order active disturbance rejection control», en *Chinese Control Conference*, IEEE, págs. 6322–6327, 2011.

[3] G., O. M., *Integracion de un Procesador Digital de Senales a una Computadora de Vuelo*, Tesis de Maestría, Universidad Autonoma de Nuevo Leon, San Nicolas de Los Garza, Nuevo Leon, Mexico, 2016.

[4] Gao, Z., «Scaling and bandwidth-parameterization based controller tuning», en *Proceedings of the American control conference*, tomo 6, págs. 4989–4996, 2006.

[5] Gonzalez-Sanchez, M., L. Amezquita-Brooks, E. Liceaga-Castro y P. Zambrano-Robledo, «Simplifying quadrotor controllers by using simplified design models», en *Conference on Decision and Control*, IEEE, págs. 4236–4241, 2013.

[6] Han, J., «From PID to active disturbance rejection control», *Transactions on Industrial Electronics*, **56**(3), págs. 900–906, 2009.

[7] Herbst, G., «A simulative study on active disturbance rejection control (ADRC) as a control tool for practitioners», *Electronics*, **2**(3), págs. 246–279, 2013.

[8] HERRICK, K., «Development of the unmanned aerial vehicle market: forecasts and trends», *Air & Space Europe*, **2**(2), págs. 25–27, 2000.

[9] JO, N. H. y H. SHIM, «Robust stabilization via disturbance observer with noise reduction», en *Control Conference (ECC), 2013 European*, IEEE, págs. 2861–2866, 2013.

[10] LURIE, B. y P. ENRIGHT, *Classical feedback control: with MATLAB*, CRC Press, 2000.

[11] NEWS, A., «DHL Drone Delivery», , 2018, URL `http://www.cbc.ca/news/technology/dhl-begins-drone-delivery-in-germany-1.2777647`.

[12] SHIM, H. y N. H. JO, «An almost necessary and sufficient condition for robust stability of closed-loop systems with disturbance observer», *Automatica*, **45**(1), págs. 296–299, 2009.

[13] TIAN, G. y Z. GAO, «Frequency response analysis of active disturbance rejection based control system», en *International Conference on Control Applications*, IEEE, págs. 1595–1599, 2007.

[14] ZULU, A. y S. JOHN, «A review of control algorithms for autonomous quadrotors», *arXiv preprint arXiv:1602.02622*, 2016.

Resumen autobiográfico

Ulises Alvarez Liceaga

Candidato para obtener el grado de
Maestría en Aeronáutica con
Orientación en Dinámica de Vuelo

Universidad Autónoma de Nuevo León
Facultad de Ingeniería Mecánica y Eléctrica

Tesis

RECHAZO ACTIVO DE PERTURBACIONES EN
VEHÍCULOS AÉREOS MULTIROTOR